ELSEVIER

Journal of Nuclear Materials 279 (2000) 234–244

journal of nuclear materials

www.elsevier.nl/locate/jnucmat

Actinide distribution in a stainless steel–15 wt% zirconium high-level nuclear waste form

D.D. Keiser Jr. [a], D.P. Abraham [b,*], W. Sinkler [a], J.W. Richardson Jr. [b], S.M. McDeavitt [b]

[a] *Argonne National Laboratory-West, P.O. Box 2528, Idaho Falls, ID 83403, USA*
[b] *Argonne National Laboratory, 9700 S. Cass Avenue, Argonne, IL 60439-4837, USA*

Received 27 October 1999; accepted 13 December 1999

Abstract

Actinide-bearing waste forms are being produced from metallic remnants resulting from the electrometallurgical extraction of uranium from EBR-II spent fuel. The baseline metal waste form (MWF) is a stainless steel–15 wt% zirconium (SS–15Zr) alloy that may contain up to 10 wt% actinides, mostly in the form of uranium. This article presents the results of scanning electron microscopy (SEM), transmission electron microscopy (TEM), and neutron diffraction on SS–15Zr alloys containing uranium, plutonium, and neptunium. Neutron diffraction results showed that the addition of uranium to SS–15Zr does not result in the formation of discrete uranium-rich phases. The lattice parameters of the $ZrFe_2$-type intermetallics are larger in uranium-containing SS–15Zr alloys and are consistent with the substitution of uranium at zirconium sites of the $ZrFe_2$ lattice. SEM studies showed that actinides are present only in the $ZrFe_2$-type intermetallics; moreover, both actinide-rich and actinide-deficient areas are found within the Laves compound. TEM showed that the simultaneous presence of multiple Laves polytypes, each with a different preference for the uranium atom, results in the uranium concentration gradients observed within the Laves intermetallics.

PACS: 61.12.Yp; 61.16.Bg; 28.41.Kw; 61.82.Bg

1. Background

The Yucca Mountain site in southern Nevada is being considered for the disposal of high-level nuclear wastes produced during nuclear reactor operation and from the treatment of spent nuclear fuel [1]. The radionuclides present in these wastes must be sufficiently isolated from the surrounding biosphere for time periods greater than ten thousand years. For geologic disposal, the following major radioisotopes are of concern: the fission products Sr-90 and Cs-137, which decay to innocuous levels within a few centuries; the long-lived fission products I-129 and Tc-99; and several long-lived isotopes of the actinide elements, U, Np, Pu, Am, and Cm [2]. A variety of waste forms (e.g., borosilicate, aluminosilicate, and phosphate glasses, silicate-based glass-ceramics, and titanate-based glass-ceramics) have been studied for the geologic disposal of high-level nuclear waste [3,4]. A technetium- and actinide-bearing metal waste form (MWF) is being produced at Argonne National Laboratory (ANL) for the disposal of metallic waste that results from the electrometallurgical treatment of experimental breeder reactor-II (EBR-II) spent fuel [5–7].

The metal waste stream from the electrometallurgical process includes cladding hulls, assembly hardware, fission products that are 'noble' to the electrorefining process, and actinide elements left behind in the anodic dissolution baskets of the electrorefiner. The waste is consolidated by melting at 1600°C under an argon atmosphere and cast into ingots. The baseline MWF for

* Corresponding author. Tel.: +1-630 252 4332; fax: +1-630 972 4406.
E-mail address: abraham@cmt.anl.gov (D.P. Abraham).

0022-3115/00/$ - see front matter
PII: S0022-3115(00)00002-7

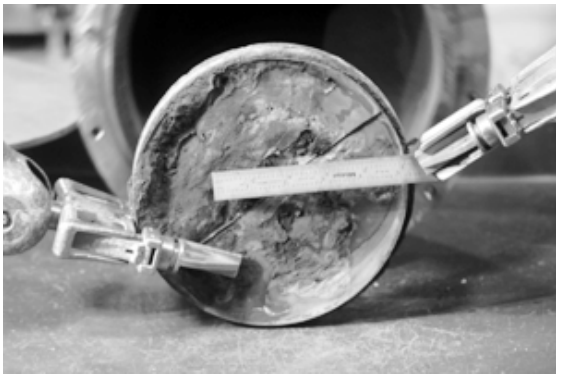

Fig. 1. Metal waste form ingot prepared from irradiated EBR-II cladding hulls.

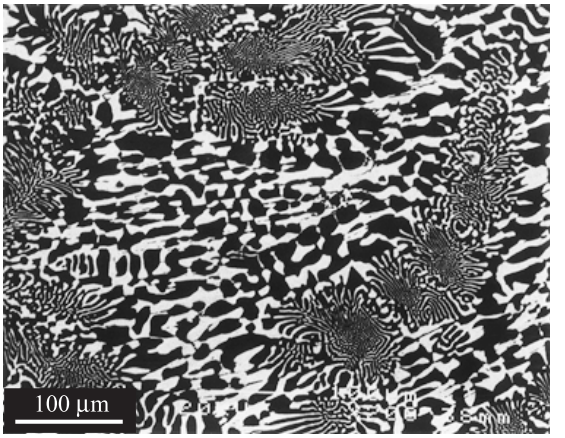

Fig. 2. Typical SEM image from an SS–15Zr alloy. The dark areas are mainly ferrite, while austenite can be seen under appropriate contrast conditions. The bright areas are $ZrFe_2$-type intermetallics.

the stainless steel-clad EBR-II fuel is a stainless steel–15 wt% Zr(SS–15Zr [1]) alloy [5]. The fission product and actinide content of the MWF depends on the fuel type (driver or blanket), fuel burnup, and the operating conditions in the electrorefiner. The nominal noble metal fission product (NMFP) content of the MWF is expected to be less than 1 wt%; nominal actinide content is expected to be ~2 wt% (mostly in the form of uranium).

A demonstration-scale hot [2] MWF ingot, cast with metallic residuals from the treatment of irradiated EBR-II driver fuel (U–10 wt% Zr), is shown in Fig. 1. The ingot is ~21 cm in diameter and ~2.5 cm thick and weighs ~5 kg; larger ingots (~30–50 kg) will be generated during the production-scale treatment of EBR-II fuel. Results of chemical analysis from core-drilled samples obtained from three demonstration-scale MWF ingots are shown in Table 1. The uranium content of the ingots ranged from ~1 to 9 wt%. The highest values observed for Np and Pu were 10 and 32 ppm, respectively. Of the NMFPs, the highest concentrations measured were for Ru (up to 0.6 wt%), Tc (up to 0.3 wt%), and Pd (up to 0.1 wt%). Other fission products, such as Mn-54 and Co-60, were present in much smaller amounts (ppb levels).

The microstructures observed in the baseline MWF alloy, SS–15Zr, have been presented in previous articles [8–10]. The alloy displays a eutectic microstructure (see Fig. 2), comprising dark areas that contain the iron solid–solution phases, ferrite and austenite, and light areas containing $ZrFe_2$-type Laves polytypes C36 (dihexagonal, $MgNi_2$-type) and C15 (cubic, $MgCu_2$-type). Small amounts of an $Fe_{23}Zr_6$-type intermetallic are also observed in an as-cast alloy. The compositions of individual phases are listed in Table 2. The Laves intermetallics contain ~24 at.% Zr, a substoichiometry of more than 25% from the expected 33.3 at.% Zr. The Ni/Cr ratio is the main compositional difference between the C36 and C15 polytypes observed in an SS–15Zr alloy: Ni/Cr ~1.5–2 for the C36 polytype and >2.5 for the C15 polytype [10]. The $Fe_{23}Zr_6$ intermetallic has a Ni/Cr ratio of ~1 and a zirconium content very close to the stoichiometric value.

The microstructures that develop in as-cast hot MWF ingots are similar to those observed in simulated [3] waste forms. The NMFP elements are contained in the SS–15Zr phases and do not form separate fission product-rich phases. The phase preferences for the various NMFP elements have been described in previous articles [6,11]. Elements such as Pd, Ru, and Rh strongly prefer the Laves intermetallics, whereas elements such as Tc are present in all phases of the SS–15Zr alloy. In backscattered electron (BSE) micrographs, the actinide elements appear as high-brightness regions within the $ZrFe_2$-type Laves intermetallics. Actinide-rich regions (containing mainly uranium) observed in a hot MWF ingot are shown in Fig. 3.

This article discusses the nature of the actinide-rich regions observed in the $ZrFe_2$-type intermetallics. Stainless steel–zirconium alloys containing up to 11 wt% actinide elements (U, Pu, and Np) were prepared and characterized by scanning electron microscopy (SEM).

[1] Alloy compositions are listed in wt%, unless noted.

[2] The term 'hot' refers to the highly radioactive ingots produced after the spent-fuel electrorefining process.

[3] Simulated waste forms refers to ingots produced by the addition of representative fission products and actinides to the SS–15Zr alloy.

Table 1
Chemical and isotopic analysis results from MWF ingots 05, 06 and 07 prepared from EBR-II cladding hulls

	05	06	07		05	06	07
Cr (wt%)	11.57	13.72	11.61	Tc (wt%)	0.11	0.32	0.31
Fe (wt%)	45.00	61.88	57.34	Total U (wt%)	*9.34*	*2.35*	*0.92*
Mn (wt%)	1.05	1.68	1.75	Total Pu (ppm)	32	6.6	3.9
Mo (wt%)	1.54	2.39	2.57	Co-60 (ppb)	383	191	457
Ni (wt%)	7.48	11.73	13.21	Mn-54 (ppb)	228	8.2	154
Pd (wt%)	0.08	0.11	0.12	Np-237 (ppm)	ND[a]	9	10
Ru (wt%)	0.17	0.66	0.62	Ru-106 (ppb)	3123	420	2999
Zr (wt%)	14.15	10.60	16.41	Sb-125 (ppb)	3212	2356	5600

[a] Not determined.

Table 2
Phase composition (at.%) obtained by energy-dispersive spectroscopy for as-cast SS–15Zr alloy sample [10]

Phase	Fe	Cr	Ni	Zr	Zr[a]	Ni/Cr
Ferrite, α	68	25	5	<0.1	–	0.2
Austenite, γ	71	19	7	<0.1	–	0.4
$ZrFe_2$-type C36	53	8	11	24	33.3	1.4
$ZrFe_2$-type C15	48	6	18	24	33.3	3
$Fe_{23}Zr_6$-type	57	10	10	20.5	20.7	1

[a] The expected Zr content at stoichiometry is shown for the intermetallic phases.

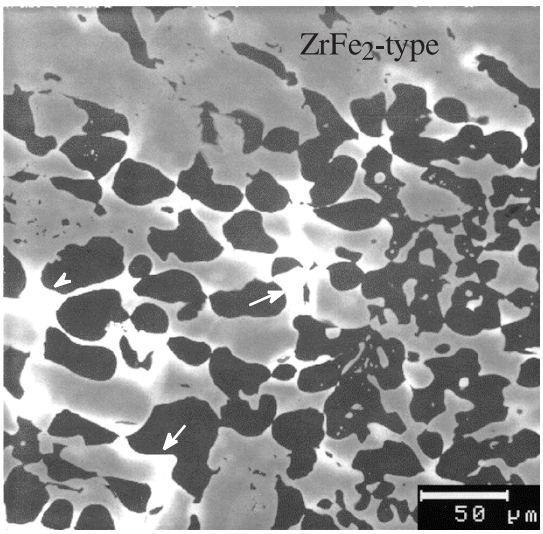

Fig. 3. Representative BSE image of a MWF sample produced from irradiated EBR-II cladding hulls. The dark areas correspond to the ferrite phase. The actinide-rich areas (marked by arrows) appear as high-brightness regions within the $ZrFe_2$-type intermetallic.

An alloy containing 5 wt% U was studied by neutron diffraction to examine the effect of uranium addition on the lattice parameters of phases present in the SS–15Zr alloy. The non-uniform distribution of uranium in the $ZrFe_2$-type intermetallics was studied by transmission electron microscopy (TEM). An understanding of actinide behavior in the SS–15Zr alloy microstructure is critical to understanding and predicting the corrosion behavior, and hence, the long-term radionuclide release from MWF ingots buried in a geologic repository.

2. Experimental

Table 3 lists the alloy compositions prepared for microstructural examination. The uranium-, plutonium, and neptunium-bearing alloys were prepared in an induction furnace. Although their anticipated content in the MWF is less than 1 wt%, the high-plutonium and neptunium alloys were generated because (1) the MWF was being considered as a plutonium-disposition alloy and (2) uranium was being examined as a microstructural surrogate for plutonium, neptunium, and other actinide elements. Alloys containing uranium and surrogate NMFP elements (Nb, Ru, Rh, Pd, and Tc) were prepared in a resistance-heated furnace to examine the effect of fission products on actinide distribution. In all cases, the metal charge was melted in yttrium oxide crucibles, held at 1600°C under flowing argon gas for 1–2 h, and slowly cooled (<10°C/min) to room temperature.

SEM was performed on samples polished through 1 μm diamond paste using a Zeiss DSM960A and an ETEC Autoscan scanning electron microscope operated in both secondary and backscattered electron modes. On the Zeiss DSM960A, phase compositions were determined by an Oxford energy-dispersive spectrometer and wavelength dispersive spectrometer, along with LINK_ISIS software. Phase compositions on the ETEC Autoscan scanning electron microscope were obtained with a Kevex 8000 (Fisons Instruments) energy-dispersive spectrometer.

Table 3
Actinide and NMFP content (wt%) of SS–15Zr alloy ingots

	U	Pu	Np	Nb	Pd	Rh	Ru	Tc
Induction furnace (~30 g ingots)	0.5	0.5	–	–	–	–	–	–
	2	2	–	–	–	–	–	–
	–	6	–	–	–	–	–	–
	–	10	–	–	–	–	–	–
	–	–	2	–	–	–	–	–
	–	6	2	–	–	–	–	–
Resistance furnace (~10 g ingots)	5	–	–	–	–	–	–	–
	5	–	–	–	–	–	–	–
	2	–	–	1	1	1	1	1
	11	–	–	–	0.1	–	0.6	0.3

TEM was performed on an SS–15Zr–5U–2Tc alloy sample using a JEOL-2010 microscope operated at 200 kV. The TEM foils were produced by slicing the samples with a diamond saw. The slices were reduced by grinding to a thickness of approximately 250 μm using 400-grit SiC paper. Following this, 3-mm disks were cut from the sections, and further mechanically-thinned to a thickness between 60 and 100 μm. The polished disks were dimpled to a central thickness of ~15 μm and then ion milled to perforation using a Gatan PIPS ion mill.

Time-of-flight (TOF) neutron diffraction data were collected from an as-cast SS–15Zr–5U alloy using the general purpose powder diffractometer at the Intense Pulsed Neutron Source (IPNS) at ANL. The TOF experiments are carried out at a fixed scattering angle, and diffraction patterns are generated as a function of incident neutron wavelength. Diffraction data are obtained at six separate detector banks, each positioned at a fixed angle relative to the incident beam. Since each detector bank views the sample from a different orientation, an assessment of preferred orientation (texture) in the sample can be obtained from variations in intensity from bank to bank. Rietveld refinements [12] were carried out on the neutron diffraction data to obtain the lattice parameters and volume content of phases observed in the sample. The influence of sample texture on Rietveld refinement calculations was minimized by averaging the results obtained from all detector banks.

3. Results

3.1. Neutron diffraction analysis

The neutron diffraction pattern obtained from the SS–15Zr–5U alloy showed peaks corresponding to five phases: ferrite, austenite, $ZrFe_2$-type polytypes C36 and C15, and an $Fe_{23}Zr_6$-type intermetallic. Diffraction peaks corresponding to discrete uranium-rich phases were not seen. The C14 polytype may have been present in the alloy but could not be definitively identified due to overlap with the C36 peaks. The basal plane dimensions of C14 and C36 are identical. The axial dimension of the C36 structure is, however, double that of C14; hence, the diffraction pattern of C36 is the same as that of C14, but with extra lines [13].

Table 4 compares the lattice parameters and amount of phases in the SS–15Zr–5U alloy with those in an as-cast SS–15Zr alloy. In the SS–15Zr–5U alloy, the lattice parameters of ferrite and austenite are identical and

Table 4
Lattice parameters and volume content (%) of phases in SS–15Zr [a] and SS–15Zr–5U alloy

Phases	Lattice parameters (nm)			Phase volume (%)		
	Alloy composition		% Change	Alloy composition		Change
	SS–15Zr	SS–15Zr–5U		SS–15Zr	SS–15Zr–5U	
Ferrite	$a = 0.2876$	$a = 0.2876$	0	40 ± 6	45	+5
Austenite	$a = 0.3596$	$a = 0.3595$	−0.028	9 ± 1	5	−4
Laves C36	$a = 0.4908$	$a = 0.4923$	0.306	33 ± 5	13	−20
	$c = 1.6016$	$c = 1.6016$	0			
Laves C15	$a = 0.6938$	$a = 0.6959$	0.303	16 ± 2	21	+5
$Fe_{23}Zr_6$	$a = 1.1690$	$a = 1.1669$	−0.18	2 ± 1	17	+15

[a] Data for SS–15Zr samples are from Ref. [8].

slightly smaller, respectively, than those in the SS–15Zr alloy. Since uranium has a larger atomic radius than the major elements in ferrite and austenite (Fe, Cr, and Ni), the observed lattice parameters suggest the absence of uranium in these iron-based solid–solution phases.

The lattice parameters of the $ZrFe_2$-type Laves intermetallic phases in the SS–15Zr–5U alloy are larger than the corresponding phases in the SS–15Zr alloy. The lattice parameter of the C15 polytype is ~0.3% larger. In the C36 polytype, parameter *a* is larger by 0.3%, whereas parameter *c* is unchanged. This indicates an anisotropic distribution of uranium within the C36 intermetallic, with the uranium atom showing a strong preference for the basal planes of the hexagonal unit cell. In contrast to the lattice expansion observed for the Laves intermetallics, Table 4 shows that the lattice parameters of the $Fe_{23}Zr_6$-type intermetallic are 0.18% smaller in the SS–15Zr–5U alloy than in the baseline SS–15Zr alloy.

The amount of the iron solid–solution phases in both SS–15Zr–5U and SS–15Zr alloys is ~50 vol%; there appears to be more ferrite but less austenite in the SS–15Zr–5U alloy. Large differences are observed in the contents of the intermetallic phases. The SS–15Zr–5U alloy contains more C15 and $Fe_{23}Zr_6$ and less C36 than the SS–15Zr alloy.

3.2. Scanning electron microscopy

3.2.1. Alloys containing uranium and NMFP elements

Typical microstructures from alloys containing uranium and NMFP elements are shown in Fig. 4; the microstructures are very similar to those observed in the hot waste forms (Fig. 3). Most of the uranium is present in high-brightness areas within the Laves intermetallics. The uranium content gradually decreases between the high-brightness areas and the adjoining areas in the intermetallic; distinct interphase boundaries are not seen.

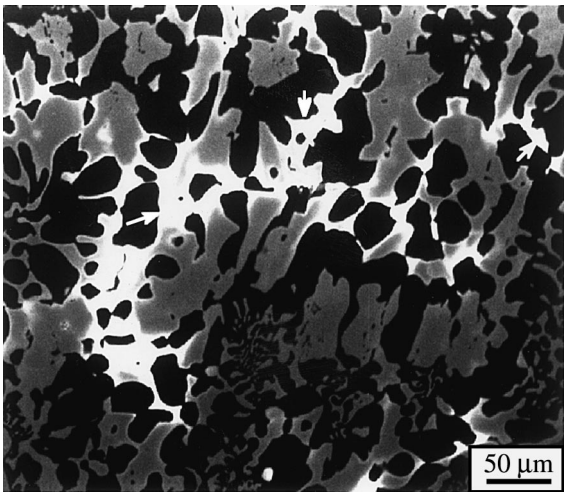

Fig. 4. BSE image from an SS–15Zr–5U alloy. The dark areas are the ferrite phase. The uranium-rich areas (marked by arrows) appear as high-brightness regions within the $ZrFe_2$-type intermetallic.

The NMFP elements are dissolved in the SS–15Zr alloy phases (as described previously) and do not affect the uranium distribution. The phase compositions from the SS–15Zr–5U, SS–15Zr–1Nb–1Ru–1Rh–1Pd–1Tc–2U, and SS–15Zr–0.6Ru–0.3Tc–0.1Pd–11U alloys are shown in Table 5. Only contents of the major alloy constituents (Fe, Cr, Ni, and Zr) and U are listed in the table.

Table 5 shows that the ferrite phase (dark areas in Fig. 4) contained negligible quantities of uranium. The austenite composition is not listed because it could not be clearly distinguished in the alloy microstructures. The high-brightness areas in the $ZrFe_2$-type intermetallic are designated as 'U-rich Laves' in Table 5. In these areas, the sum of uranium and zirconium contents ranged from ~23 to 27 at.%, and the Ni/Cr ratio ranged from 5.8 to

Table 5
Phase compositions [a] for SS–15Zr samples containing uranium and NMFP elements

Alloy composition	Possible phase	Composition, at.% (±2 at.%)				
		Fe	Cr	Ni	Zr	U
SS–15Zr–5U	Ferrite	67.5	23.2	5	Neg.[a]	Neg.
	U-rich Laves	44.9	3.3	25.7	7.6	17.2
	Other Laves [b]	49.1	6	18	20.6	1.5
SS–15Zr–1Nb–1Pd–1Rh–1Ru–1Tc–2U	Ferrite	67.6	22.3	3.5	Neg.	Neg.
	U-rich Laves	43.2	3.3	22.5	10.9	12.2
	Other Laves	46.5	4.1	17.9	19.1	3
SS–15Zr–0.1Pd–0.6Ru–0.3Tc–11U	Ferrite	65.9	26.8	3.1	Neg.	Neg.
	U-rich Laves	49.3	3.1	18	8	19.3
	Other Laves	53.3	6.5	12.1	21.9	2.7
	$Fe_{23}Zr_6$-type	58.1	11	9.5	17.2	1.7

[a] Negligible.
[b] The designation 'Other Laves' represents areas in the Laves intermetallic away from the U-rich regions.

7.8. The areas in the $ZrFe_2$-type intermetallic farther away from the high-brightness regions are designated as 'Other Laves' in Table 5. In these areas, the sum of uranium and zirconium contents ranged from ~22 to 25 at.%, and the Ni/Cr ratio ranged from 1.9 to 4.4.

In the SS–15Zr alloy, the $Fe_{23}Zr_6$-type intermetallic is identified by its distinct morphology and a zirconium content that is close to the stoichiometric value of 20.7 at.%. Clear identification of this phase in the uranium-bearing alloys proved to be difficult, probably because the high-brightness areas masked the differences in phase morphology. The phase was identified in the SS–15Zr–0.6Ru–0.3Tc–0.1Pd–11U alloy and contained 17.2 at.% zirconium, which is lower than the expected stoichiometric content. Table 5 shows that the sum of uranium and zirconium content in the phase is 18.9 at.%. The Ni/Cr ratio is 0.9, similar to that observed in the baseline SS–15Zr alloy.

3.2.2. Alloys containing uranium, plutonium, and neptunium

The actinide distribution in SS–15Zr alloys containing uranium, plutonium, and neptunium is shown in Table 6. The microstructures of these alloys were similar to those shown in Fig. 4. For all alloys, the actinide elements were concentrated in high-brightness areas within the $ZrFe_2$-type intermetallic; increasing the alloy actinide content resulted in a higher volume fraction of these areas. The maximum actinide concentration in these areas is not definitively known, but concentrations up to 20 at.% are shown in Table 6.

The sum of actinide and zirconium contents in the high-brightness areas of alloys without neptunium ranged from 25 to 27 at.%; in Np-bearing alloys, the sum was 21 at.%. The Ni/Cr ratio in the high-brightness areas was high and ranged from 7.3 to 17. In the $ZrFe_2$-type intermetallic away from the high-brightness areas, the Ni/Cr ratio ranged from 1.7 to 3. The sum of actinide and zirconium contents in these Other Laves areas ranged from ~23 to 24 at.%, except in neptunium-containing alloys where it ranged from 13.5 to 14.5 at.%.

The microstructure was unchanged in an SS–15Zr–10Pu alloy that was heat-treated at 851°C for 100 h. The plutonium did not redistribute to attain a uniform composition in the intermetallic nor did any plutonium-bearing phases precipitate during this heat treatment. However, the annealing temperature may have been insufficient to allow significant diffusion that could have resulted in elemental redistribution within the Laves intermetallic.

3.3. Transmission electron microscopy

Selected area diffraction patterns (SADPs) from the four Laves polytypes that were observed in the SS–15Zr–5U–2Tc alloy are shown in Figs. 5(a)–(d). These polytypes are the two- and four-layer hexagonal structures (*Strukturbericht* designation C14 and C36), the three-layer cubic structure (*Strukturbericht* designation C15), and a six-layer hexagonal structure (6H), which has been observed for $Zr(Fe,Cr)_2$ precipitates in Zircaloy-4 [14]. The EDS spectra corresponding to these polytypes are shown in Figs. 6 (a)–(d). The spectra show the U-$L_{\alpha 1}$ and Zr-$K_{\alpha 1}$ characteristic lines at 13.615 and 15.747 keV, respectively. There was a pronounced variation in the relative peak intensities of these peaks

Table 6
Phase compositions for actinide-bearing SS–15Zr alloys

Alloy	Possible	Composition (±2 at.%)						
Composition (wt%)	Phase	Fe	Cr	Ni	Zr	U	Pu	Np
SS–15Zr–2U–2Pu	Ferrite	74	21	3	1	0.2	0.2	–
	Actinide-rich Laves	49	3	22	12	9	5	–
	Other Laves[a]	57	7	13	22	0.5	0.5	–
SS–15Zr–6Pu	Ferrite	71	24	4	1	–	0.2	–
	Actinide-rich Laves	38	3	34	8	–	17	–
	Other Laves	55	8	14	22	–	1	–
SS–15Zr–10Pu	Ferrite	70	25	3	1	–	0.5	–
	Actinide-rich Laves	35	2	34	7	–	20	–
	Other Laves	55	7	14	22	–	2	–
SS–15Zr–2Np	Ferrite	71	23	5	0.4	–	–	0.5
	Actinide-rich Laves	42	3	34	6	–	–	15
	Other Laves	58	7	21	13	–	–	0.5
SS–15Zr–6Pu–2Np	Ferrite	70	24	5	0.5	–	0.4	0.1
	Actinide-rich Laves	46	3	30	6	–	10	5
	Other Laves	60	8	17	13	–	1	0.5

[a] The designation 'Other Laves' represents areas in the Laves intermetallic away from actinide-rich regions.

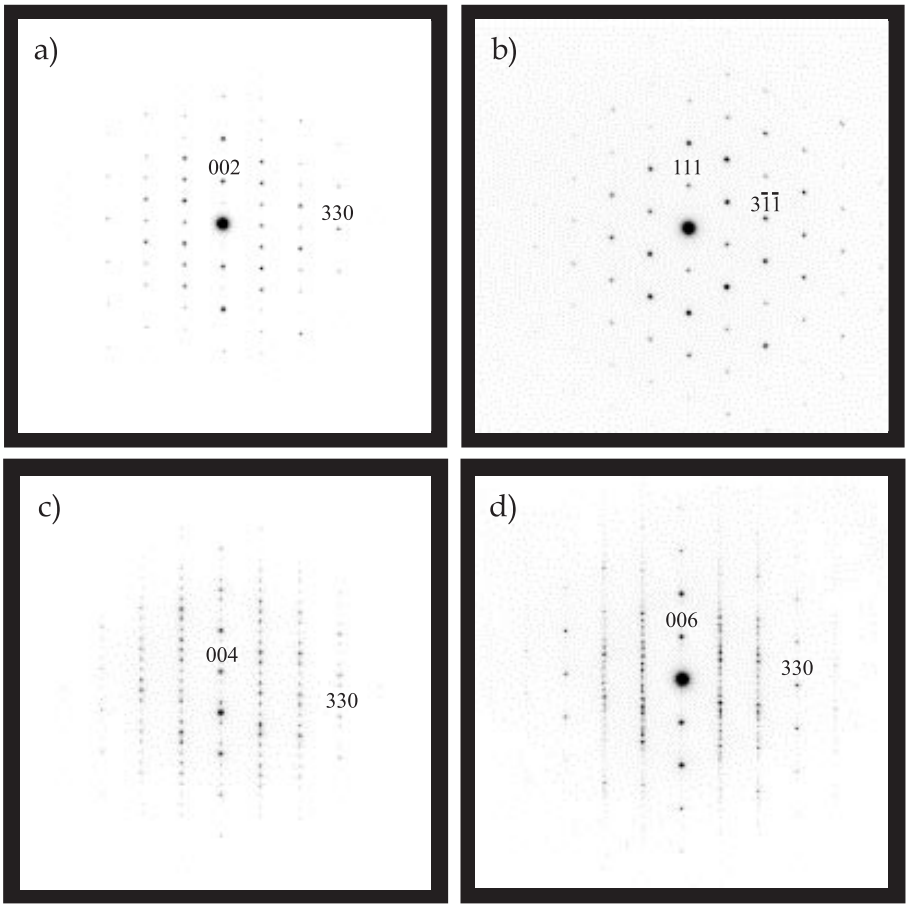

Fig. 5. SADPs from a SS–15Zr–5U–2Tc alloy containing four different Laves polytypes, perpendicular to the primary stacking direction (vertical in figures): (a) C14, (b) C15, (c) C36, and (d) 6H. For hexagonal polytypes, this is the *c*-axis, which is equivalent to (1 1 1) in the case of C15.

for the different polytypes; the cubic C15 structure consistently showed a larger relative intensity of the U-$L_{\alpha 1}$ line than the other (hexagonal) polytypes.

According to the Cliff–Lorimer ratio technique [15], the relative concentrations of uranium and zirconium are given by

$$\frac{x_U}{x_{Zr}} = k_{U,Zr}\frac{I_U}{I_{Zr}}, \tag{1}$$

where x_U and x_{Zr} are the concentrations of uranium and zirconium, respectively, I_U and I_{Zr} are the integrated intensities of characteristic EDS lines of uranium and zirconium, respectively, and $k_{U,Zr}$ is the Cliff–Lorimer factor, which may be obtained using a standard. Table 7 shows a number of measurements of I_U/I_{Zr}, I_{Fe}/I_{Cr}, I_{Fe}/I_{Ni}, and I_{Ni}/I_{Cr} from several areas in which the polytype could be positively identified using selected area diffraction. Since no standard was available to determine the value of $k_{U,Zr}$, the actual relative concentrations are not known.

Table 7 shows that the I_U/I_{Zr} values are highest for the C15 (0.18–0.46) and lowest for the C14 polytype (0.04–0.09). The other polytypes, C36 and 6H, show intermediate I_U/I_{Zr} values (0.08–0.12). These results indicate that uranium atoms show the strongest preference for the C15 polytype and the weakest for the C14 polytype. The cubic character of a Laves polytype increases in this order: C14, 6H, C36, and C15 [16]. It is evident from Table 7 that uranium shows a greater preference for Laves polytypes with the most cubic character. The area richest in uranium (position 1 in Table 7) was immediately adjacent to the ferrite phase; this is consistent with SEM observations, which show that uranium tends to segregate to the edges of the Laves intermetallics.

In addition to variations in uranium concentration, Table 7 shows that the uranium-rich cubic C15 areas

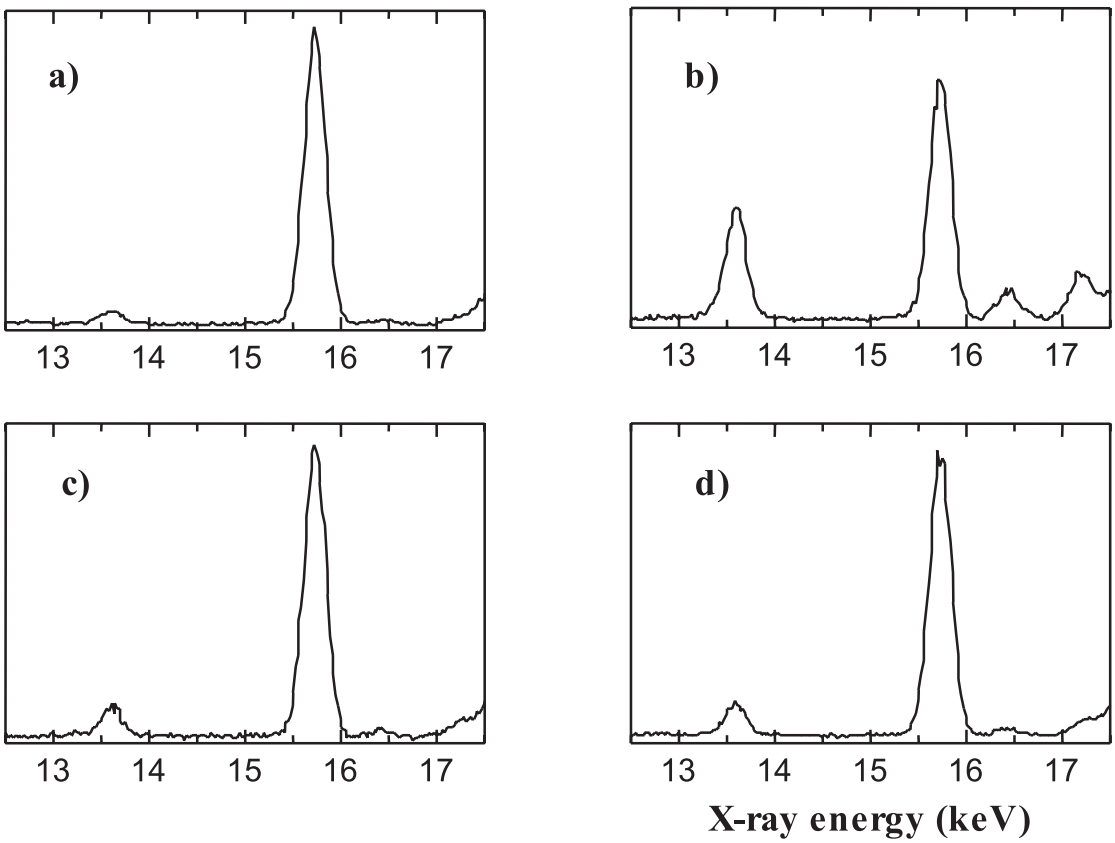

Fig. 6. Portions of TEM-EDS spectra from a SS–15Zr–5U–2Tc alloy showing the intensity of the U-$L_{\alpha 1}$ (13.615 keV) and Zr-$K_{\alpha 1}$ (15.747 keV) characteristic lines from areas corresponding to Figs. 5 (a)–(d). The crystal structures were identified by transmission electron diffraction: (a) C14, (b) C15, (c) C36, and (d) 6H.

contain more Fe and Ni relative to Cr, whereas the zirconium-rich hexagonal C14 areas contain the most Cr. The Ni/Cr intensity ratio is highest for the C15 polytype (2.3–3.8) and lowest for the C14 polytype (1.1–1.5). The C36 and 6H polytypes show intermediate Ni/Cr intensity ratios (1.3–1.9). The measured Ni/Cr intensity ratios agree with the Ni/Cr concentration ratios previously measured on the baseline SS–15Zr alloy (see Table 2).

Table 7
Intensity ratios for various elements observed in the $ZrFe_2$-type Laves polytypes

Position	Structure	I_U/I_{Zr}	I_{Fe}/I_{Cr}	I_{Fe}/I_{Ni}	I_{Ni}/I_{Cr}
1	C15	0.461	11.42	2.98	3.82
2	C15	0.179	8.84	3.90	2.27
3	C15	0.312	9.08	3.65	2.49
4	C36	0.083	6.67	5.02	1.33
5	C36	0.107	7.85	4.56	1.77
6	C36	0.106	8.40	4.34	1.93
7	C36	0.108	8.04	4.35	1.85
8	C36	0.113	7.97	4.19	1.90
9	6H	0.120	7.66	4.57	1.67
10	6H	0.114	7.96	4.31	1.85
11	C14	0.037	6.22	5.44	1.14
12	C14	0.067	7.06	4.79	1.47
13	C14	0.035	6.10	5.82	1.05
14	C14	0.092	6.87	4.62	1.49

4. Discussion

4.1. Actinide effects in the Laves intermetallics

The presence of actinide-rich regions in the Laves intermetallics was the main microstructural difference between actinide-containing and actinide-free SS–15Zr alloys. The proportion of the actinide-rich regions increased with increased actinide addition to the baseline alloy. SEM/EDS analysis showed that the brightest areas in the $ZrFe_2$-type intermetallics contained the highest concentration of actinides and the darkest areas contained the lowest. No clear phase boundaries were

observed between the actinide-rich and the actinide-deficient areas. Instead, actinide-concentration gradients were observed within a single Laves compound phase.

Concentration gradients are not expected within an alloy phase under equilibrium conditions. The existence of actinide-concentration gradients in the $ZrFe_2$-type intermetallics may be due to the nonequilibrium conditions associated with the cooling of an as-cast alloy. Alternatively, the observed concentration gradients may be due to the presence of a quasi-continuous series of Laves polytypes, each with a different preference for the actinide elements. These polytypes can be formed from each other by the insertion of ordered stacking defects, accomplished by migration of Shockley partial dislocations [16,17]. In the SS–15Zr–5U alloy, the simultaneous presence of four Laves polytypes (C14, 6H, C36, and C15), along with the preference of uranium for polytypes with the most cubic character (C15, for example), may explain the uranium-enrichment and concentration gradients observed in the Laves intermetallics.

In SS–15Zr alloys, the $ZrFe_2$-type phase is substoichiometric in zirconium and contains ~24 at.% Zr [8,10]. In the uranium-bearing SS–15Zr alloys, the sum of uranium and zirconium contents in the $ZrFe_2$-type intermetallic ranges from 22 to 25 at.%, which suggests the substitution of uranium at the zirconium sublattice of the intermetallic. The substitution of uranium at the Zr-sites is reasonable because both elements form Laves compounds with iron [18,19]. The main difference between these Laves compounds is that UFe_2 forms at the stoichiometric value of uranium, whereas $ZrFe_2$ exhibits a homogeneity range mainly on the iron-rich side. Bruckner studied the substoichiometric $ZrFe_2$ phase and concluded that iron atoms occupy zirconium sites in binary Fe–Zr alloys [20]. In SS–15Zr alloys, the zirconium sublattice of the $ZrFe_2$ intermetallics may be either randomly or preferentially occupied by Fe, Cr or Ni, the other major elements in the alloy; constitutional vacancies are unlikely to account for the ~25% substoichiometry observed in these intermetallics.

The lattice parameters of the $ZrFe_2$-type intermetallic phases in the SS–15Zr–5U alloy are larger than the corresponding phases in the SS–15Zr alloy. The C15 phase lattice parameter and lattice parameter a of C36 are both 0.3% larger in the uranium-containing alloy. On first inspection, it appears that uranium substitution at zirconium sites can not account for this observation since the metallic radius [4] of uranium is smaller than that of zirconium [21,22]; hence, a close-packed hard-sphere model would predict that the lattice would contract. However, the published lattice parameters for the binary compounds UFe_2 and $ZrFe_2$ are 0.7061 [23] and 0.704 nm [24], respectively, indicating that uranium has a larger atomic size than zirconium in the chemical environment of an iron-based Laves compound. Thus, the observed lattice expansions fully agree with the predominant substitution of uranium on zirconium sites in the Laves intermetallics.

TEM examination showed that the uranium-rich C15 areas also contained more Fe and Ni, whereas the zirconium-rich hexagonal C14 areas contained the most Cr. A possible explanation for this behavior relates to electronic effects induced by atomic substitutions in the Laves compound. For example, the substitution of Ni at the A- (or B-) sites may alter the electronic concentrations such that the C15 phase is stabilized; similarly, the substitution of Cr may result in the stabilization of the C14 phase. The relationship of electronic concentration effects (electron-to-atom ratio) to Laves phase polytype stability has been discussed by other investigators [13,25].

Thermodynamic considerations of phase stability offer another possible explanation for the observed elemental preference in the Laves polytypes. For instance, some investigators have suggested that the enthalpy of formation of a Laves compound can be used as a measure of its stability [26,27]. The preference of chromium for the zirconium-rich hexagonal Laves polytypes may be correlated to observations from the U–Cr and Zr–Cr binary phase diagrams [18,28]. In the U–Cr binary, the absence of intermediate phases suggests that the enthalpy of mixing is small and possibly positive, whereas the formation of stable $ZrCr_2$ compounds formed in the Zr–Cr binary suggests at least a negative (exothermic) enthalpy of formation. Similarly, the preference of nickel for the uranium-rich cubic polytype may be related to the strongly exothermic heats of formation observed in the U–Ni and Zr–Ni binary system [18,29].

In SEM micrographs (Fig. 3, for example), the actinide-rich areas are frequently found at the edges of the Laves intermetallics, in close proximity to the ferrite phase. This phenomenon may be qualitatively explained by relating alloy solidification to solidification characteristics observed in the Fe–Zr and Fe–Cr–Zr phase diagrams [19,30]. The high melting temperatures of the $ZrCr_2$ and $ZrFe_2$ compounds suggest that a uranium-deficient $Zr(Fe,Cr_2)$-type compound with a C14 crystal structure [14,31] initially solidifies from the melt. On approaching the eutectic temperature, the phase is gradually enriched in uranium, resulting in the formation of the 6H and C36 polytypes. At the eutectic temperature, the ferrite coprecipitates with the uranium-enriched C15 Laves compound, which results in the close association of the ferrite and actinide-rich areas observed in the SEM images.

Although extensive TEM investigation was conducted only on a uranium-bearing alloy, the effect of

[4] Since Laves phases exhibit predominantly metallic bonding, the metallic atom radius is used to evaluate the relevance of atom size factors on the occurrence and stability of phases.

plutonium on the Laves compounds is believed to be similar. The existence of the $PuFe_2$ Laves compound [18] and the sum of plutonium and zirconium contents, ~25 at.%, suggest that plutonium substitutes at the Zr-sites of the $ZrFe_2$ compound. Similarly, since neptunium is known to form the $NpFe_2$ Laves compound in the Fe–Np binary [18], it would be reasonable to assume that the element substitutes at the Zr-sites. However, in neptunium-bearing SS–15Zr alloys, the sum of actinides and zirconium is only ~13.5 at.% in actinide-deficient regions of the Laves compound and ~21 at.% in the actinide-rich areas. The anomalous behavior of neptunium in SS–15Zr may be related to the immiscible character of the Np–Zr binary [32], which is distinctly different from the U–Zr and Pu–Zr systems [18] that are characterized by complete high-temperature solid-state miscibility. Previous investigators have indicated that the role of 5f electrons may be particularly pronounced in the alloying behavior of neptunium-bearing systems because the degree of 5f bonding is maximized in this element [33,34].

4.2. Actinide effects on other alloy phases

The Fe–U, Fe–Pu, and Fe–Np phase diagrams [18] show that the ferrite (α) phase has negligible solubility for the actinide elements, which agrees with the SEM–EDS results listed in Tables 5 and 6. The increase in ferrite content observed in the SS–15Zr–5U alloy (see Table 4) is related to the decrease in the amount of austenite, which is destabilized by the affinity of the Laves intermetallics for Ni. The small lattice contraction observed in the ferrite and austenite phases of the SS–15Zr–5U alloy may be due to a minor depletion of chromium from these phases.

Although SEM–EDS identification of the $Fe_{23}Zr_6$-type phase was difficult in the actinide-bearing alloys, peaks corresponding to the phase were clearly observed in the neutron diffraction patterns. The Rietveld refinement results (Table 4) show that the phase undergoes a lattice contraction of 0.18% in a SS–15Zr alloy with 5 wt% uranium. Furthermore, the amount of the $Fe_{23}Zr_6$-type phase increased by 15 vol.%, suggesting that the phase is stabilized by uranium addition. The uranium effects on the phase are larger than those suggested by the SEM–EDS data (Table 5), which shows that the phase contains only 1.7 at.% U. Further characterization is needed to clarify the effects of uranium on the $Fe_{23}Zr_6$-type phase.

5. Conclusions

The distribution of actinide elements in the SS–15Zr microstructure was studied by the preparation of alloys that contained up to 11 wt% U, 10 wt% Pu, and 6 wt% Np. The phases observed in the actinide-bearing alloys were similar to those observed in the baseline SS–15Zr alloy. SEM examination showed that the actinides were concentrated in certain (high-brightness) areas of the $ZrFe_2$-type Laves intermetallic and that a gradual decrease in actinide content between the high-brightness and the adjoining areas in the intermetallic occurred. The simultaneous presence of several polytypes, along with the preference of actinide elements for individual polytypes, has been proposed to explain the presence of actinide-rich regions and concentration gradients observed in the Laves intermetallics.

The behavior of actinides in the SS–15Zr alloys may be summarized as follows.

1. Uranium appears to substitute at Zr-sites of the $ZrFe_2$-type intermetallics. SEM–EDS data show that the sum of uranium and zirconium contents in the intermetallics is ~23–25 at.%, which, although sub-stoichiometric is similar to the zirconium behavior observed in the baseline SS–15Zr alloy.
2. TEM examination revealed the presence of four Laves polytypes in the SS–15Zr–5U alloy: C14, 6H, C36 and C15. Uranium showed the strongest preference for the C15 polytype and the weakest preference for the C14. The preference of uranium for a Laves polytype depends on the degree of the polytype's cubic character.
3. The lattice parameters of Laves phases in the SS–15Zr–5U alloy are larger than those of the corresponding phases in the SS–15Zr alloy. The observed lattice expansions agree with uranium substitution at zirconium sites of the $ZrFe_2$ intermetallics.
4. The amount of C15 and $Fe_{23}Zr_6$ is larger in the SS–15Zr–5U alloy than in the SS–15Zr alloy, indicating that the phases are stabilized by the presence of uranium.
5. Plutonium behavior is similar to that of uranium; the element appears to substitute at Zr-sites of the $ZrFe_2$-type intermetallic. Hence, uranium may be considered as a microstructural surrogate for plutonium.
6. The SEM–EDS data show compositional differences in the Laves phases of the neptunium- and uranium-bearing SS–15Zr alloys. It is unclear from this study whether uranium can be used as a microstructural surrogate for neptunium.

Acknowledgements

The US Deptartment of Energy supported this work under contract W-31-109-Eng-38. We acknowledge the assistance of R. Elliott, S.G. Johnson, and S.M. Frank in preparing the actinide-bearing alloys and thank M.C. Petri for heat-treating the SS–15Zr–10Pu alloy. This work has benefited from the use of the Intense Pulsed

Neutron Source at Argonne National Laboratory. This facility is funded by the US Department of Energy, BES-Materials Science, under contract W-31-109-ENG-38.

References

[1] Department of Energy, DOEs Yucca Mountain Studies, Yucca Mountain Site Characterization Project of Civilian Radioactive Waste Management, Washington, D.C, 1992.
[2] K.B. Krauskopf, Radioactive Waste Disposal and Geology, Chapman and Hall, New York, 1988, 12–29.
[3] W. Lutze, R.C. Ewing, Radioactive Waste Forms for the Future, North-Holland, Amsterdam, 1988.
[4] I.W. Donald, B.L. Metcalfe, R.N.J. Taylor, J. Mater. Sci. 32 (1997) 5851.
[5] S.M. McDeavitt, D.P. Abraham, J.Y. Park, J. Nucl. Mater. 257 (1998) 21.
[6] D.P. Abraham, D.D. Keiser, Jr., S.M. McDeavitt, in: International Conference on Decommissioning and Decontamination and on Nuclear and Hazardous Waste Management, vol. 2, American Nuclear Society, LaGrange Park, IL, 1998, p. 783.
[7] D.D. Keiser, R.D. Mariani, J. Nucl. Mater. 270 (1999) 3.
[8] D.P. Abraham, J.W. Richardson Jr., S.M. McDeavitt, Mater. Sci. Eng. A 239–240 (1997) 658.
[9] D.P. Abraham, S.M. McDeavitt, J.Y. Park, Metall. Mater. Trans. A 27 (1996) 2151.
[10] D.P. Abraham, J.W. Richardson Jr., in: G.E. Fuchs, K.A. Dannenann, T.C. Derugon (Eds.), Long Term Stability of High Temperature Materials, TMS, Warrendale, PA, 1999, p. 169.
[11] D.D. Keiser, Jr., D.P. Abraham, J.W. Richardson Jr., J. Nucl. Mater. 277 (2000) 333.
[12] A.C. Larson, R.B. Von Dreele, Los Alamos National Laboratory Report LAUR 86-748, 1986.
[13] R.P. Elliot, W. Rostoker, Trans. ASM 50 (1958) 617.
[14] X.Y. Meng, D.O. Northwood, J. Less Common Met. 125 (1986) 33.
[15] D.B. Williams, C.B. Carter, Transmission Electron Microscopy, vol. II, Plenum, New York, 1996.
[16] X. Meng Burany, D.O. Northwood, J. Less Common Met. 170 (1991) 27.
[17] C.W. Allen, K.C. Liao, Phys. Stat. Sol. A 74 (1982) 673.
[18] M.E. Kassner, D.E. Peterson, (Eds.), Phase Diagram of Binary Actinide Alloys, ASM International, Materials Park, OH, 1995.
[19] H. Okamoto, (Ed.), Phase Diagram of Binary Iron Alloys, ASM International, Materials Park, OH, 1993.
[20] W. Bruckner, K. Kleinstuck, G.E.R. Schulze, Phys. Stat. Sol. A 23 (1967) 475.
[21] F. Laves, Theory of Alloy Phases, ASM, Cleveland, OH, 1956, p. 124.
[22] A.E. Dwight, Trans. ASM 53 (1961) 479.
[23] G. Katz, A.J. Jacobs, J. Nucl. Mater. 5 (1962) 338.
[24] M.S. Granovsky, D. Arias, J. Nucl. Mater. 229 (1996) 29.
[25] D.I. Bardos, K.P. Gupta, P.A. Beck, Trans. AIME 221 (1961) 1087.
[26] J.H. Zhu, C.T. Liu, L.M. Pike, P.K. Liaw, Metall. Mater. Trans. A 30 (1999) 1449.
[27] G.M. Campbell, Metall. Trans. A 8 (1977) 1493.
[28] D. Arias, J.P. Abriata, Bull. Alloy Phase Diagrams 7 (1986) 237.
[29] P. Nash, C.S. Jayanath, Bull. Alloy Phase Diagrams 5 (1984) 144.
[30] V. Raghavan, Phase Diagram of Ternary Iron Alloys, Part 6B, Indian Institute of Metals, Calcutta, 1992, p. 1094.
[31] O. Canet, M. Latroche, F. Bouree-Vigneron, A. Percheron-Guegan, J. Alloys Comp. 210 (1994) 129.
[32] J.K. Gibson, R.G. Haire, J. Nucl. Mater. 201 (1993) 225.
[33] J.K. Gibson, R.G. Haire, T. Ogawa, J. Nucl. Mater. 273 (1999) 139.
[34] L. Brewer, The Cohesive Energy of the Elements, Lawrence Berkeley Laboratory Report LBL-3720, CA, 1977.